Post-perihelion photometry of dust grains in the coma of 67P Churyumov–Gerasimenko

Elisa Frattin, Gabriele Cremonese, Emanuele Simioni, Ivano Bertini, Monica Lazzarin, Theresa Ott, Esther Drolshagen, Florangela La Forgia, Holger Sierks, Cesare Barbieri, et al.

Monthly Notices
of the
ROYAL ASTRONOMICAL SOCIETY

MNRAS **469,** S195–S203 (2017)
Advance Access publication 2017 June 8

doi:10.1093/mnras/stx1395

Post-perihelion photometry of dust grains in the coma of 67P Churyumov–Gerasimenko

E. Frattin,[1,2]★ G. Cremonese,[1] E. Simioni,[1,3] I. Bertini,[2] M. Lazzarin,[2] T. Ott,[4] E. Drolshagen,[4] F. La Forgia,[2] H. Sierks,[5] C. Barbieri,[2] P. Lamy,[6] R. Rodrigo,[7,8] D. Koschny,[9] H. Rickman,[10,11] H. U. Keller,[12] J. Agarwal,[5] M. F. A'Hearn,[13,5] M. A. Barucci,[14] J.-L. Bertaux,[15] V. Da Deppo,[3] B. Davidsson,[10] S. Debei,[16] M. De Cecco,[17] J. Deller,[5] S. Ferrari,[18] F. Ferri,[18] S. Fornasier,[14] M. Fulle,[19] A. Gicquel,[5] O. Groussin,[20] P. J. Gutierrez,[21] C. Güttler,[5] M. Hofmann,[5] S. F. Hviid,[22] W.-H. Ip,[23] L. Jorda,[20] J. Knollenberg,[22] J.-R. Kramm,[5] E. Kührt,[22] M. Küppers,[24] L. M. Lara,[21] J. J. Lopez Moreno,[21] A. Lucchetti,[1,18] F. Marzari,[2] M. Massironi,[25] S. Mottola,[22] G. Naletto,[3,18,26] N. Oklay,[5] M. Pajola,[18,27] L. Penasa,[18] X. Shi,[5] N. Thomas,[28] C. Tubiana[5] and J.-B. Vincent[5]

Affiliations are listed at the end of the paper

Accepted 2017 June 3. Received 2017 May 29; in original form 2017 March 30

ABSTRACT

We present a photometric analysis of individual dust grains in the coma of comet 67P/Churyumov–Gerasimenko using OSIRIS images taken from 2015 July to 2016 January. We analysed a sample of 555 taken during 18 d at heliocentric distances ranging between 1.25 and 2.04 au and at nucleocentric distances between 80 and 437 km. An automated method to detect the tracks was specifically developed. The images were taken by OSIRIS NAC in four different filters: Near-IR (882 nm), Orange (649 nm), FarOrange (649 nm) and Blue (480 nm). It was not always possible to recognize all the grains in the four filters, hence we measured the spectral slope in two wavelengths ranges: in the interval [480–649] nm, for 1179 grains, and in the interval [649–882] nm, for 746 grains. We studied the evolution of the two populations' average spectral slopes. The data result scattered around the average value in the range [480–649] nm, while in the [649–882] nm we observe a slight decreasing moving away from the Sun as well as a slight increasing with the nucleocentric distance. A spectrophotometric analysis was performed on a subsample of 339 grains. Three major groups were defined, based on the spectral slope between [535–882] nm: (i) the steep spectra that may be related with organic material, (ii) the spectra with an intermediate slope, likely a mixture of silicates and organics and (iii) flat spectra that may be associated with a high abundance of water ice.

Key words: methods: data analysis – techniques: photometric – comets: general – zodiacal dust.

1 INTRODUCTION

The *Rosetta* spacecraft orbited around Jupiter family comet 67P/Churyumov–Gerasimenko for 2 yr, reaching distances from the nucleus smaller than 10 km. For the first time in the history of space missions a spacecraft arrived so close to a comet, allowing observations of the development of the inner coma from inside. During this time range, the Optical, Spectroscopic and Infrared Remote Imaging System (OSIRIS by Keller et al. 2007) mapped the coma from different configurations, providing a detailed understanding of its nature. The large amount of OSIRIS images clearly revealed the presence of individual dust grains, characterizing the overall coma (Davidsson et al. 2015; Fulle et al. 2015). We focused our investigation on these single grains.

In the past, a coma of icy grains was revealed on Hartley 2 by Kelley et al. (2013) that, for the first time, detected and analysed single objects of cm-size in a comet's coma. The *Rosetta*

★ E-mail: elisa.frattin@gmail.com

spacecraft permitted a more detailed study of dust grains. For instance, Fulle et al. (2016) derived a dust size distribution consistent with a differential power-law index of −4 for sizes >1 mm and with a power index of −2 for sizes <1 mm at 2 au. During the perihelion passage, the index decreased to −3.7, indicating a major contribution of grains smaller than 1 mm. An estimation of the masses of cm-size grains is given by Ott & Drolshagen et al. (this volume), finding values ranging between 10^{-6} and 10^{-2} kg on a sample of more than 200 particles.

Dust analysis shows that several complex processes work on the grains, driving their release and changing their behaviour. The increasing activity at short heliocentric distances corresponds to a larger dust grains ejection rate. Such grains are accelerated by gas drag and rocket force due to sublimation of the ice (Agarwal et al. 2016; Gicquel et al. 2016), and undergo different fates: part of them exceeds escape velocity (about 1 m s^{-1}) and leaves the cometary coma (Thomas et al. 2015), while another part falls back on the surface (Kramer & Noack 2015; La Forgia et al. 2015; Lai et al. 2016). Aeolian structures like ripples or dunes are related to this process and to the surface dust transport (Thomas et al. 2015). The dynamics involved in the releasing, and eventually in the falling back, depends on several grains properties as their shapes and rotational state, intimately related with the gas production rate (Fulle et al. 2015).

A deeper knowledge of the dust nature, through the study of physical and compositional properties of single grains, allows a better understanding of the relationship with the nucleus and the mechanisms involved in the ejection.

In this work, we present a spectrophotometric analysis of a wide sample of dust grains, which provides some possible hints on the grain composition. The colour characteristics of single grains were previously measured by Cremonese et al. (2016) on a sample of 70 grains, finding a spectral slope value peaked between 12 and 16 per cent/100 nm in the wavelength range [480–743 nm]. They also measured a negative spectral slope for 16 grains, associated with the presence of water ice. Now, a larger amount of data and the information coming from an extended range of filters allow to realize a more accurate statistics to describe them.

2 DETECTION METHOD

The large amount of data obtained by OSIRIS (including the dust grains observations), required us to develop an automatic routine able to identify and to analyse the particle tracks present in several images, corresponding to the passage of the particles during the time of integration.

The main aim of this program is to detect the grains tracks and their orientation in the reference system of the image. At the same time it can analyse the point-by-point intensities of the grains tracks as well, thus providing their light curves. The latter show pieces of evidence in some cases of periodic oscillations, corresponding to rotating grains Duda & Hart (1973).

The detection of the tracks can be performed taking advantage of a similarity function, a window-based matching function, commonly used in photogrammetry to define the homologues between two images. Dust track features can be easily modelled and the match between the model and the image is a valid probability operator for the presence of the dust grain.

Dust tracks can be modelled by two parameters: their orientation Φ in the reference system of the image and their full width at half-maximum, here approximated with a mean value of 1 px. For each orientation (considered with a sampling of 4°), a squared

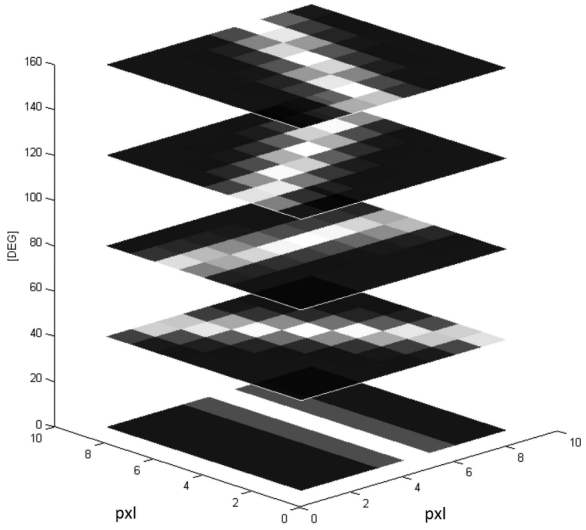

Figure 1. Subset of templates used to model the tracks. For each orientation, with 4° angular step, a template representing the synthetic trail is defined.

window (classically defined as template T^{Φ}) representing the trail can be synthetically generated simply using a rect convolved with a bi-dimensional Gaussian (representing both the grain and the instrument point spread function). An image representing a subset of templates is shown in Fig. 1. This bench of templates can be used to detect at the same time the presence and the orientation of the tracks by using, as similarity function, the normalized cross correlation (NCC). The NCC is invariant to local mean and standard deviation, it means it is not influenced by star variability or signal variation. For each orientation Φ the NCC between the template T^{Φ} and the image is computed as

$$SM^{\Phi}_{(i,j)} = I \overline{\otimes} T^{\Phi}. \quad (1)$$

The similarity map $SM^{\Phi}_{(i,j)}$ associates to each pixel coordinates and to a defined orientation Φ the probability to find a track in this location with the considered orientation.

Relative standard deviation (RSD) indicates the ratio between the effective mean signal (with respect to the background) and the standard deviation of the noise. The usage of NCC allows to reach a detection probability of 90 per cent also in the case of a RSD of 1.75. In fact, given an angle Φ, the presence of a track influences the similarity function of the pixels (i,j) along the direction Φ. This correlation can be detected convolving any level of the $SM^{\Phi}_{(i,j)}$ with the same template function T^{Φ}, which represents a mono-directional low pass filter in the direction considered:

$$SM^{\Phi\prime} = I' \overline{\otimes} T^{\Phi} \otimes T^{\Phi} \quad (2)$$

allows to increase the performance of the detection (by imposing continuity of the track along its orientation, even where different tracks overlap). Segmentation process (isocurves based on Boolean morphological operators) allows at this point to extract the tracks distinguished by their orientation. This information can be used to avoid fake tracks. An example of the final detection is shown in Fig. 2.

3 OBSERVATIONS

We focused our analysis on images taken in the post-perihelion period, i.e. from the end of August 2015 to January

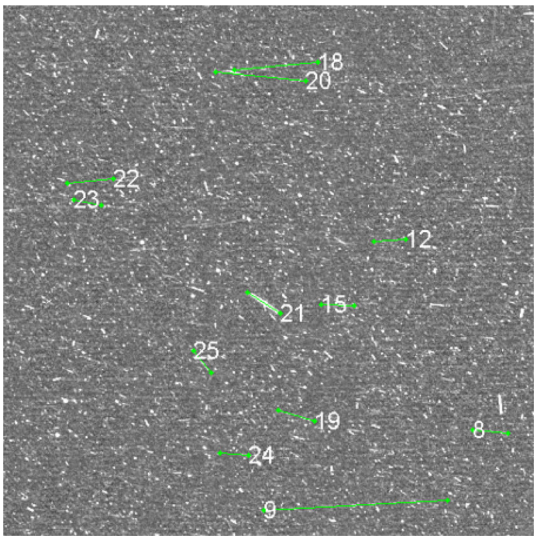

Figure 2. Final step of the detection on a portion of a NAC image. The detected tracks are identified with a number.

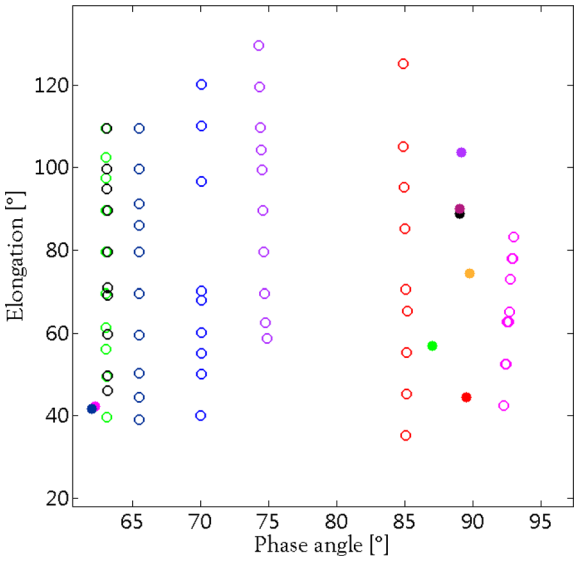

Figure 3. The empty circles represent the geometry of the sequences taken at different Sun elongation (i.e. the angle formed by the Sun-spacecraft and spacecraft-coma region directions) keeping fixed the phase angle. The filled circles represent the images taken with both phase angle and elongation fixed. The colours indicate different set of observations.

2016 (two sequences were taken before the perihelion). The images were chosen from the series devoted to grain colour (GC) and grain track (GT) acquired by the NAC (narrow angle camera) in four different filters: Near-IR ($\lambda = 882.1$ nm, bandwidth $= 65.9$ nm), FarOrange ($\lambda = 649.7$ nm, bandwidth $= 84.5$ nm), Orange ($\lambda = 649.7$ nm, bandwidth $= 84.5$ nm) and Blue ($\lambda = 400$ nm, bandwidth $= 74.9$ nm). The difference between FarOrange and Orange filters lies in the presence of a focusing plate: the first one focuses from infinity to 2 km, while the second one from 2 to 1 km (Tubiana et al. 2015). These two types of series were taken with different observational geometries. In GC data set the camera scans the coma in the Sun-comet-spacecraft plane at a fixed phase angle α (i.e. the angle formed by the Sun-comet and comet-spacecraft directions). In the GT data set, the camera orientation remains fixed, so observing always the same coma region. The angles describing the above mentioned configurations are shown in Fig. 3, where the empty circles refer to GC images and the filled ones to GT. In total, we analysed 555 images taken during 18 d at heliocentric distances ranging between 1.25 au and 2.04 au and at distances from the nucleus between 80 and 437 km (one set being taken at 1220 km). The entire data set is reported in Table 1.

In each image we identified two types of grains: those in bound orbits with the nucleus and those outflowing. The bound grains appeared as faint dots in the background, far from the spacecraft, while the outflowing grains appeared as tracks and are closer to the spacecraft (Rotundi et al. 2015). To estimate the distance at which the camera is still able to detect a particle we used the equation by Agarwal et al. (2016):

$$\Delta = \sqrt{I_\odot \frac{s^2 p \phi(\alpha)}{J r_\mathrm{h}^2}} \tag{3}$$

where Δ is the distance of the grain from the camera, $I_\odot = 1.565$ W m^{-2} nm^{-1} is the solar flux at 1 au in the Orange NAC filter (F22), s is the grain size in m, p the albedo, $\phi(\alpha)$ is the phase function of the coma, J is the flux of the aggregate in W m^{-2} nm^{-1} sr^{-1} and r_h is the heliocentric distance measured in au. In Table 2, we report the maximum distance Δ at which the camera is able to observe an aggregate of dimension s, extended on a 4 pixels area. Clearly this quantity depends on the object's composition and on the illumination's conditions. We considered, as reference, the lower value of radiance measured for a grain $J = 10^{-7}$ W m^{-2} nm^{-1} sr^{-1}. Since the dust material is supposed to be dark, we used two values for the albedo: 0.04 and 0.1. The phase function is that determined by Fornasier et al. (2015) for the nucleus at 90°, $\phi = 0.02$. During the period of our analysis the spacecraft was at heliocentric distances ranging between 1.3 au at perihelion and 2 au on 2016 January, so we used an average value of $r_\mathrm{h} = 1.5$ au for our estimates. As an example of the camera sensitivity, we obtain from equation (3) that the camera is able to resolve an aggregate of 1 cm with low albedo at a range of 20 km.

Generally, the images were taken in groups of 3 or 4, following the filter sequence: Near-IR, FarOrange, Orange, Blue. The exposure time was 12.5 s and the gap between two observations was about 11 s, short enough to follow the grain motions in more than one image. In fact, we were able to detect a large amount of grains: 746 with Near-IR and Orange and 1179 with Orange and Blue. Most of the grains we detected with the first two filters are not the same we found with the last two. However, there were 339 cases in which we could find the same grain in all the filters. We will describe them in Section 4.

4 COLOURS OF THE GRAINS

In order to characterize the photometric properties of the dust grains, we measured their spectral slopes using the formula by Jewitt & Meech (1986):

$$S = \frac{I/F_\mathrm{Red} - I/F_\mathrm{Blue}}{\lambda_\mathrm{Red} - \lambda_\mathrm{Blue}} \frac{20\,000}{I/F_\mathrm{Red} + I/F_\mathrm{Blue}} \tag{4}$$

where I/F is the reflectance of the grain in the two filters, with I the radiance of the object and F the solar flux, λ is the central wavelength of the filter. The spectral slope S is expressed in units of per cent/100 nm.

To perform a statistical analysis, we decided to consider the data set collected on the same day as a group, even if they were taken at different phase angles. These correspond to assume that

Table 1. Observational dataset. MTP: medium term planning (1 month); STP: short-term planning (1 week); Type: grain colours or grain track; *rc*: nucleocentric distance; r_h: heliocentic distance; α_N: phase angle of the nucleus; ϵ_{Sun}: Sun elongation; $\#_{649-882}$: number of grains detected with Near-IR and FarOrange filters; $\#_{480-649}$: number of grains detected with Orange and Blue filters; $\#_{spectra}$: number of spectra.

MTP	STP	Type	Epoch	*rc* (km)	r_h (au)	$\alpha_N(^\circ)$	$\epsilon_{Sun}(^\circ)$	$\#_{649-882}$	$\#_{480-649}$	$\#_{spectra}$
018	066	GC	2015-07-24	183	1.26	90	91	41	51	27
019	067-2	GC	2015-08-04	238	1.25	89	45	52	82	28
019	070-3	GC	2015-08-25	403	1.25	85	35–125	29	29	2
020	071-3	GC	2015-08-31	404	1.26	70	40–120	38	59	6
020	073-1	GC	2015-09-11	326	1.31	119	29	9	19	5
020	073-4	GC	2015-09-15	327	1.31	92	40–85	8	13	2
021	075-2	GC	2015-09-28	1220	1.37	50	20–90	26	43	9
021	078-4	GC	2015-10-18	437	1.47	65	40–110	35	58	14
022	079-1	GC	2015-10-23	389	1.51	63	40–110	62	83	21
022	081-2	GC	2015-11-06	244	1.61	63	45–110	70	91	32
022	081-3	GT	2015-11-10	201	1.63	63	43	83	108	24
022	082-4	GT	2015-11-17	141	1.68	62	42	57	136	47
023	083-1	GC	2015-11-19	126	1.70	74	60–130	30	44	9
023	083-1	GT	2015-11-27	144	1.70	88	58	31	49	15
023	086-3	GT	2015-12-10	99	1.86	89	104	57	101	39
023	085-5	GC	2015-12-14	100	1.90	89	90	78	116	25
024	087-1	GT	2015-12-17	99	1.90	89	75	26	49	16
024	089-2	GT	2016-01-04	80	2.04	89	90	50	82	18

phase reddening in the dust coma was negligible. Actually, on the surface of the nucleus, a variation of the spectral slope of about 0.1 per cent deg^{-1} was measured in the range of phase angle of [1.3–52°] and in the wavelength range of [535–882] nm (Fornasier et al. 2015). This effect has been attributed to the multiple scattering, due to the roughness of the surface, and it becomes more important at large phase angles. However, for what concerns the dust coma, we do not expect any significant correlation between the reflectivity gradient and the phase angle (Jewitt & Meech 1986). In fact, the coma of the comet is effectively optically thin, likely composed by absorbent material with a low albedo, supporting the assumption that the multiple scattering is not an important contribution (Fink & Rinaldi 2015).

Bertini et al. (this volume) studied the variations of the coma colours as function of phase angle and deduced that the single scattering is the dominant process on the 67P coma. Therefore, measured colours are not affected by a systematic effect depending on the geometry of observation. Under this assumption, we could derive the spectral slope for all the grains detected and group them depending on the dates.

We measured the spectral slopes of 1179 grains in the wavelengths range [480–649] nm and 746 in the range [649–882] nm. The two populations represent a different sample, since it was not always possible to identify the same grain in all the filters. A subset of 339 grains was recognized in the four filters and will be analysed in Section 5. An example of our results is shown in Figs 4 and 5. The histograms represent the number of grains with certain values of spectral slope for both the wavelengths ranges. These data were taken on 2015 October. The grain distribution appears spread around a central peak, with spectral slope that ranges from negative to large positive values. Therefore, we decided to fit it with a Gaussian normalized to the total counts, which provided a statistic value for the means and the errors. The standard error of the mean was computed as $se = \sigma/\sqrt{N}$, where σ is the standard deviation of the Gaussian distribution and N the number of grains for which the spectral slope was measured. This type of analysis was performed for the whole set of images, finding the average values with the relative errors for each day of the sample. The results are reported in Table 3. On

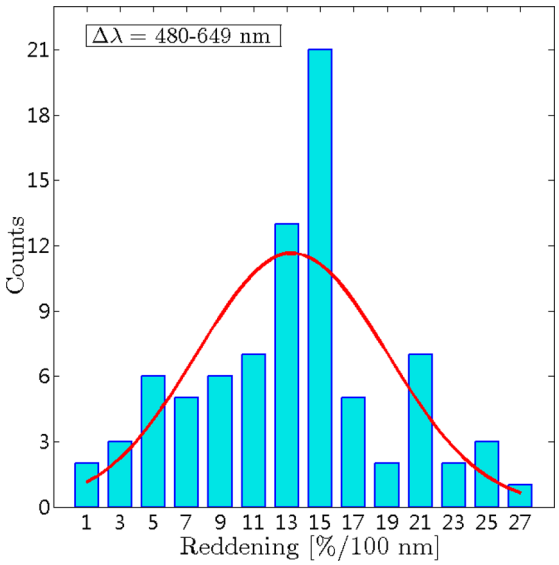

Figure 4. Spectral slope distribution in the range Orange and Blue on 2015 October. The distribution is fitted with a Gaussian, normalized to the area of the histogram.

average, we found a spectral slope of 12.9 ± 0.2 per cent/100 nm in the range Orange Blue and of 7.3 ± 0.2 per cent/100 nm in the range Near-IR Orange. The two slopes are different also for the normalization used: at about 550 nm for the first one and at about 770 nm for the second one.

These results describe a general behaviour of the grains in the coma. Therefore, we can infer that the bulk of the grain population has a steeper spectral slope in the blue part of the spectrum and a flatter spectral slope in the red part of the spectrum.

It is interesting to note that sometimes the distributions extend also in the region of negative values. We found about 6 per cent of grains have spectral slope <0 in the range [480–649] nm and about 8 per cent in the range [649–882] nm. High abundance of water ice,

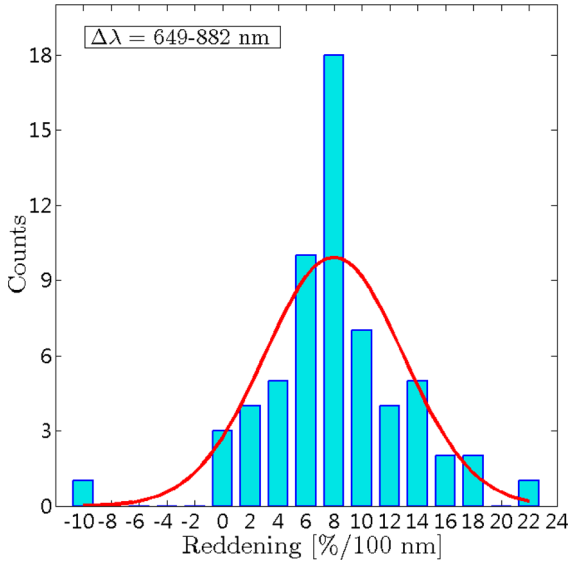

Figure 5. Spectral slope distribution in the range Near-IR and Orange on 2015 October. The distribution is fitted with a Gaussian, normalized to the area of the histogram.

Table 2. Maximum distance Δ at which the camera is able to observe an aggregate of dimension s, according to equation (3). The dimension s is related to the albedo p and to the phase function ϕ. The values are obtained considering a radiance $J = 10^{-7}$ W m^{-2} nm^{-1} sr^{-1} at heliocentric distance $r_h = 1.5$ au.

s(m)	p	Δ(km)
10^{-2}	0.04	20
10^{-3}	0.04	2.0
10^{-6}	0.04	0.0020
10^{-2}	0.10	31
10^{-3}	0.10	3.1
10^{-6}	0.10	0.0031

for instance, is associated with neutral or negative values of spectral slope (Rotundi et al. 2015; Fornasier et al. 2016; Oklay et al. 2016).

Therefore, for those grains presenting low or negative spectral slope values in both wavelengths intervals, we can infer a water ice composition. Also the presence of silicates could justify a negative value in the range [649–882] nm (DeMeo & Carry 2013).

4.1 Evolution of spectral slope

In order to analyse the possible variations of the spectral slopes with time, we studied the evolution with respect to the heliocentric and nucleocentric distances. The images analysed in this work were taken with different geometry of acquisition and with a nucleus distance ranging between 100 km and 400 km. Assuming that the camera was able to see GTs up to the distance of 10–20 km (see Table 2), it has been possible to characterize the grain populations at relative distances from the nucleus, even if we do not know the real distance of the dust grains from the spacecraft.

Figs 6 and 7 show the values of the average spectral slope measured for each sequence.

The data result scattered within the values of 11.6–15.8 per cent/100 nm in the range [480–649] nm (blue points), but no particular trend is revealed. This peculiar variability was observed also by Bertini et al. (this volume), in the trend of the spectral slope of the overall coma in a similar wavelength range. In fact, they measured a slope of 11–14 per cent/100 nm between 376 and 744 nm. The evolution of the spectral slope in the range [649–882] nm shows variations as well, within the values of 5.3–8.8 per cent/100 nm (red points), but on average it seems to decrease moving away from the Sun, and to increase with the distance from the comet.

Therefore, the red part of the spectrum seems to be more sensitive to the changes the grains undergo. Since the spectral slope computed up to 744 nm does not reveal any significative trend with respect to the distances, we expect that the characteristic feature responsible for the increasing or decreasing spectral slope lies between [744–882] nm. This variability may hint at a certain degree

Table 3. Values of average spectral slope in the range of wavelengths [480–649] nm and in the range [649–882] nm with associated standard errors (se). Each measurement refers to a specific epoch.

Epoch	$S_{480-649}$	se	$S_{649-882}$	se
2015-07-24	15.8	0.9	7.8	0.5
2015-08-04	12.9	0.7	6.8	0.5
2015-08-25	12.8	1.5	6.9	0.8
2015-08-31	12.4	0.9	8.8	0.4
2015-09-11	12.8	1.3	7.7	1.0
2015-09-15	13.5	1.3	8.5	1.3
2015-09-28	13.1	1.0	8.7	0.7
2015-10-18	14.6	1.9	7.7	0.7
2015-10-23	13.5	0.6	7.5	0.4
2015-11-06	11.6	0.7	8.3	0.5
2015-11-10	11.9	0.9	7.4	0.5
2015-11-17	11.8	0.6	7.3	0.5
2015-11-19	14.2	0.9	6.4	0.7
2015-11-27	12.0	0.8	7.4	0.6
2015-12-10	12.0	0.6	6.7	0.3
2015-12-14	12.0	0.8	7.2	0.5
2015-12-17	13.2	0.8	5.4	0.6
2016-01-04	12.9	0.7	5.3	0.4

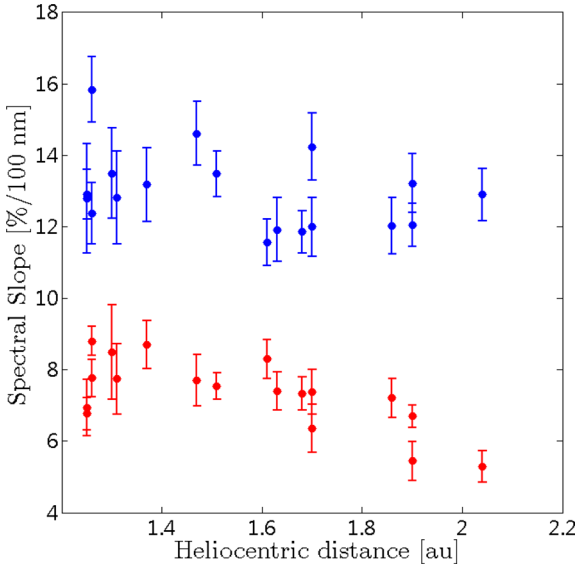

Figure 6. Daily average spectral slopes between [649–882] nm (red) and between [480–649] nm (blue) versus heliocentric distance. The standard errors of the mean (se $= \sigma/\sqrt{N}$) are associated with each measurement.

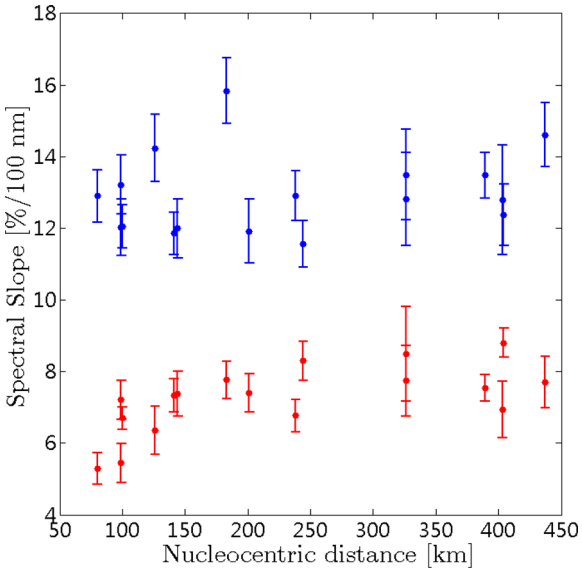

Figure 7. Daily average spectral slopes between [649–882] nm (red) and between [480–649] nm (blue) versus nucleocentric distance. The standard errors of the mean (se $= \sigma/\sqrt{N}$) are associated with each measurement.

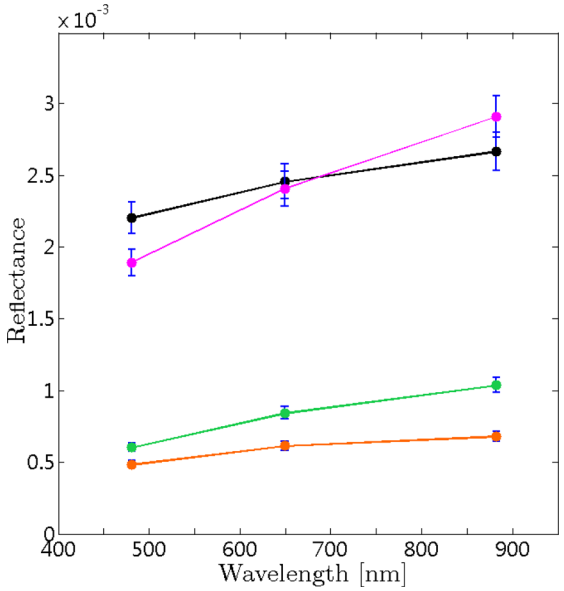

Figure 8. 3-point spectra of four grains taken on 2015 November. The black one is supposed to be a grain composed by water ice. Indeed, the high reflectance and the flat spectrum are two conditions associated with the presence of water ice in the aggregate.

of heterogeneity in the coma properties, depending on the on-going evolution of the comet's environment.

5 SPECTROPHOTOMETRY

To better characterized the grains composition, we performed also the spectrophotometric analysis of the grains. Indeed, when the time interval between two consecutive images was sufficiently short, we were able to identify the same grain in the four filters. Overall, we derived 339 3-point spectra. An example is reported in Fig. 8.

The flux's value in each filter was obtained integrating all the track's signal. Since it can show fluctuations due to the grain spin, we

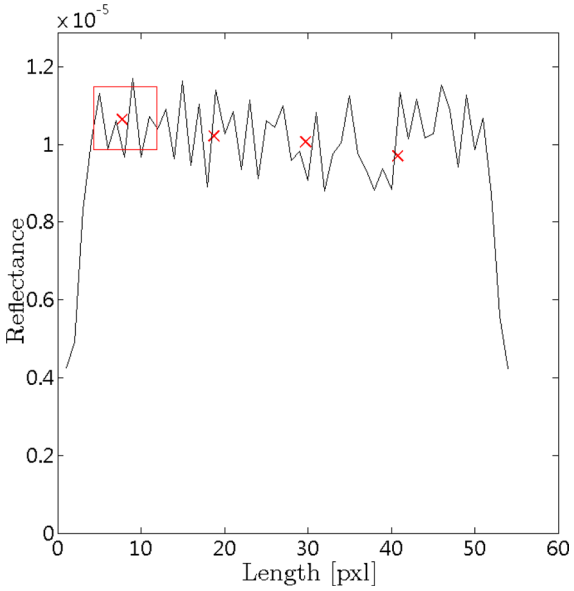

Figure 9. Light-curve profile obtained from the track of a rotating grain acquired with the WAC. The red box highlights the part of WAC curve corresponding to simultaneous NAC track. The red star points show the average values of the flux measured in the box interval.

measured an estimate of this effect. We analysed a sample of WAC (wide angle camera) images taken simultaneously to the NAC ones with F21 Green filter (537 nm, bandwidth = 63.2 nm). Their long exposure time (90 s) covered four NAC images (12.5 s), allowing to quantify the track luminosity's changes that possibly occurred. The statistics was performed on 200 tracks belonging to images taken on 2015 August and September. A typical light curve of an aggregate taken with the WAC is shown in Fig. 9. To be consistent with the NAC's exposure time intervals, we divided the WAC tracks signal into two groups: the one corresponding to the NAC images and the one corresponding to the time interval between consecutive shots. Then, we measured the mean reflectance and the variance for the intervals corresponding to the NAC images.

It resulted that the most probable value for the error, in terms of flux's average percentage, was about 5 per cent. Assuming a comparable filters' sensitivity we could apply a variability of about 5 per cent on the flux's measurements even for the other NAC filters.

We basically identified three types of spectra: (a) very steep slope spectra, (b) spectra with intermediate slope values and (c) spectra presenting a flat slope trend. The same spectra of Fig. 8 are shown in Fig. 10 in terms of relative reflectance.

Moreover, we decided to measure the spectral slope of the sub-sample of grains between Green and Near-IR, [535–882] nm, with the following formula, reported by Fornasier et al. (2015):

$$S = \frac{I/F_{882} - I/F_{535}}{I/F_{535}(882-535\,\mathrm{nm})} 10\,000, \quad (5)$$

I/F is the reflectance of the grain, with I the radiance of the object and F the solar flux.

This is a slight different wavelength interval with respect to the previous measurements, usually applied at the nucleus analysis. Indeed, this choice allows a further consistent comparison with the nucleus surface, which will be discuss in the next section.

Since we do not have measurements with the Green filter, we decided to fit the 3-point spectra with a linear interpolation. Then, we extrapolated the values of the spectra at the required wavelengths

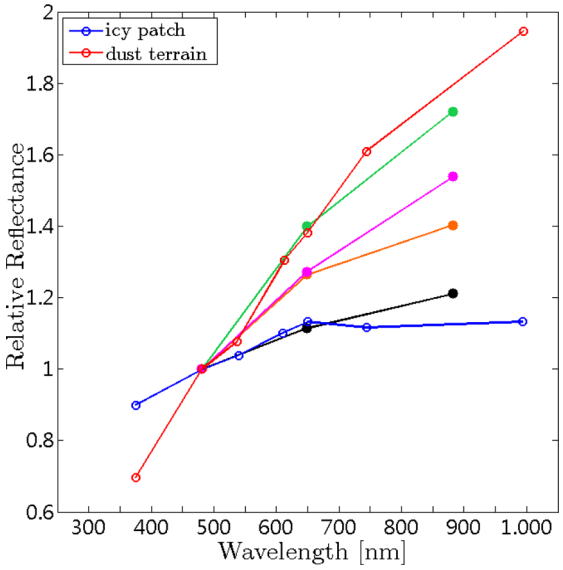

Figure 10. Normalized spectra of the same four grains of Fig. 8. They are superimposed to two terrains on the nucleus. In red, a dust terrain and in blue an ice patch ($\alpha = 90°$). The steepest spectrum (green) is related with the dust terrain and probably mostly composed by organics; the two intermediate spectra (pink and orange) are associated with a mixture of organics and silicates and the flatter spectrum (black) is similar to the one of icy patch on the surface of the nucleus and likely composed by water ice.

Table 4. Daily average spectral slope computed for 339 grains in the wavelength range [535–882] nm. The standard error of the mean se is associated.

Epoch	$S_{535-882}$	se
2015-07-24	11.3	1.4
2015-08-04	10.3	0.9
2015-08-25	23.3	1.5
2015-08-31	11.4	0.8
2015-09-11	6.6	1.5
2015-09-15	13.4	2.3
2015-09-28	10.5	1.6
2015-10-18	11.3	0.9
2015-10-23	9.9	0.7
2015-11-06	10.6	1.0
2015-11-10	10.5	1.5
2015-11-17	9.1	0.8
2015-11-19	10.0	0.6
2015-11-27	9.0	1.2
2015-12-10	11.2	1.1
2015-12-14	9.6	0.9
2015-12-17	10.9	0.6
2016-01-04	9.4	1.1

and measured the spectral slope between 535 and 882 nm for the 339 grains of the sample. We measured an average value for the spectral slope of 11±3 per cent/100 nm, quite in agreement with the values of the overall coma found by Bertini et al. (this volume), which range between 11 and 14 per cent/100 nm. The result is inconsistent also with the values of about 11 per cent/100 nm obtained by Ott & Drolshagen et al. (this volume) on a sample of more than 100 single grains. The values of the average spectral slope computed for each day, with relative statistical errors, are reported in Table 4.

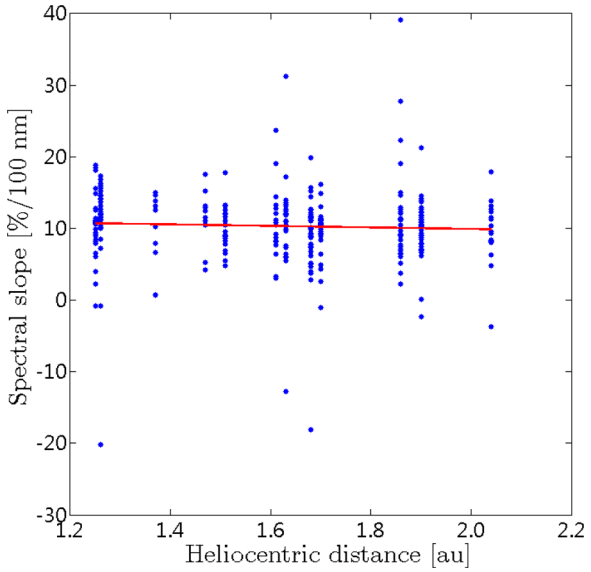

Figure 11. Spectral slopes between [535–882] nm versus the heliocentric distance. Each blue point represents the spectral slope obtained from the 3-point spectra fit.

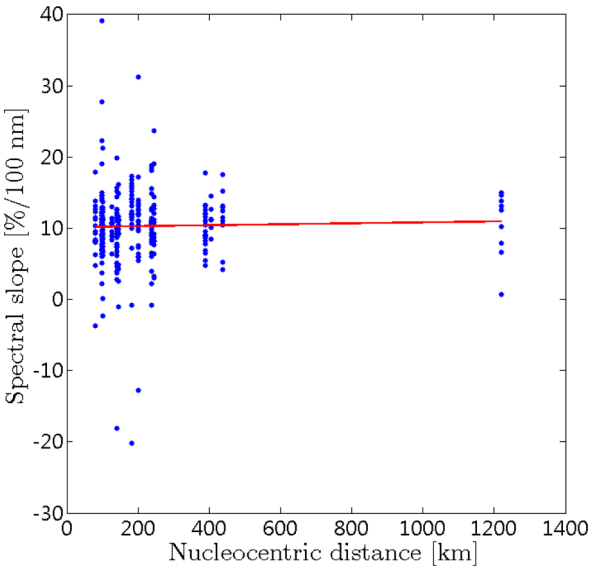

Figure 12. Spectral slopes between [535–882] nm versus the nucleocentric distance. Each blue point represents the spectral slope obtained from the 3-point spectra fit.

Then, we analysed the spectral slope with respect to the heliocentric and nucleocentric distances. Few data set were not statistically relevant so we neglected them (i.e. those taken on August 25, on September 11 and on September 15). The results are shown in Figs 11 and 12. Each point represents the spectral slope obtained with equation (5) for the 339 grains of the subsample. We found that the average values of spectral slope, measured for each day, do not follow any particular trend with these distances.

5.1 Comparison with the nucleus

To check the nature of the dust grains, we compared the 3-point spectra with the spectra of several nucleus terrains. We took as

reference the nucleus terrains spectra taken at phase angle 90°, provided by Barucci et al. (2016), where a distinction has been done between dust terrains and icy patches. Following the results by Fornasier et al. (2015) for low heliocentric distances, the nucleus undergoes a phase reddening effect. This produces an increasing of the spectral slope of about 5 per cent/100 nm for phase angle varying from 0° to 60°. On the contrary, the dust is not affected by any phase reddening. Our analysis and consequent nucleus-dust comparison is therefore applicable for nucleus parameters obtained with a phase angle $\alpha = 90°$.

We found that (see Fig. 10) the first type of spectrum, the ones with the highest value of spectral slope, well fits the spectral behaviour of nucleus dust terrains, and might be composed by organics (Pommerol et al. 2015). The second type instead, could be associated with a mixture of silicates and organics. Spectra of S-type asteroids show a peak around 0.7 μm and an absorption band around 1 μm due to olivine. Since we do not have sensitivity between 600 and 900 nm, we are not able to observe the peak and we see only a neutral trend or a low positive slope (DeMeo & Carry 2013). The measurement done by Cremonese et al. (2016) may strengthen this hypothesis. In fact, they found a red slope of 16 per cent/100 nm between blue (480.7 nm) and red (743.7 nm) filters, implying that the intensity might grow until the peak associated with the silicates around 700 nm and then decreases.

Finally, the flat type seems to superimpose to the spectrum of the icy patch. Usually we expect to see icy grains with flat spectrum and high reflectance (black spectrum in Figs 8 and 10), but we found also grains with flat trend and low reflectance. Since we were not able to estimate the absolute distance from the nucleus, we may have observed small particle of ice very far from the spacecraft. Assuming that the water ice sublimation depends on the nucleus distance and on the ejection time, we do not expect to see a large amount of water ice in the coma (Gicquel et al. 2016). Alternatively this third type of flat spectra might represent carbonaceous material with very low albedo (DeMeo & Carry 2013).

Moreover, we considered the laboratory experiments of Pommerol et al. (2015) and Poch et al. (2016) to test the sublimation of water ice mixed with silicates and organic material. They found that such mixture changed its spectral slope during the sublimation process. Starting from a flat spectrum, they demonstrated that, after just 10 h, the trend of the spectrum changed, becoming steeper. At the end of the experiment, the resulting spectrum could be related to a very pristine organic material.

Since the grains were ejected with a velocity of the order of few m s^{-1} (Rotundi et al. 2015), they needed about 1 d to arrive at more than 100 km from the nucleus when we observed them. Therefore, the three types of spectra we measured could represent different phases of an on-going sublimation process active on the grains themselves.

Another approach to interpret the different grain spectra was based on the spectral slope classification. A correspondence between surface features and values of the spectral slope was introduced by Fornasier et al. (2015) and Oklay et al. (2016).

We decided to arrange the grains into three categories, consistently with the spectra types we defined earlier. The relative composition of the grains is estimated to be: organics in the case of great values of spectral slope (>15 per cent/100 nm), a mixture of organics and silicates in the intermediate interval (5–15 per cent/100 nm) and ices or carbonaceous material in the case of lowest values (<5 per cent/100 nm). The results are resumed in Table 5. The intermediate group is the most populated.

Table 5. Percentage of grain populations, grouped for different range of spectral slope [derived by (5)], and relative possible composition.

Population (per cent)	Spectral slope (per cent/100 nm)	Composition
10	<5	Water ice/carbonaceous material
77	5–15	Mixture of silicates and organics
13	>15	Organics

6 CONCLUSIONS

We analysed the photometric behaviour of the grains in the coma of 67P in the time range from 2015 July and 2016 January. We extracted geometric and photometric parameters with an automatic method specifically developed. The results can be summarized as follows:

(i) We measured the average spectral slope of the grains for each set of images obtaining the total average value of 12.9 ± 0.2 per cent/100 nm in the range [480–649] nm and 7.3 ± 0.2 per cent/100 nm in the range [649–882] nm.

(ii) We analysed the reddening in the two wavelength ranges with respect to the heliocentric and nucleocentric distances. We revealed a variability in the behaviour of the spectral slope that could hint at heterogeneity in the coma due to physical processes affecting the released material.

(iii) We performed a spectrophotometric analysis of 339 grains observed in three filters (Blue, Orange and Near-IR). We divided the spectra into three major groups:

(a) steep, which may be connected with the presence of organics, with a slope values >15 per cent/100 nm;

(b) intermediate, which are supposed to be a mixture of silicates and organics, corresponding to a slope range between 5 and 15 per cent/100 nm;

(c) flat, most likely due to much higher abundance of water ice, that should be suitable for a comet, but in case of very low albedo grains we have to mention a possible higher abundance of carbonaceous material.

(iv) We found an average value for the spectral slope of the grains subsample of about 11 per cent/100 nm in the wavelength range [535–882] nm. No trend of the spectral slope with respect to the heliocentric and nucleocentric distances was measured.

(v) We compared the spectra with two characteristic terrains of the nucleus, finding a correspondence between the steeper spectra and the dust terrain, while the flatter one is compatible with the icy patch.

ACKNOWLEDGEMENTS

OSIRIS was built by a consortium of the Max-Planck-Institut für Sonnensystemforschung in Göttingen, Germany; CISAS-University of Padova, Italy; the Laboratoire d'Astrophysique de Marseille, France; the Instituto de Astrofísica de Andalucia, CSIC, Granada, Spain; the Research and Scientific Support Department of the European Space Agency, Noordwijk, The Netherlands; the Instituto Nacional de Técnica Aeroespacial, Madrid, Spain; the

Universidad Politéchnica de Madrid, Spain; the Department of Physics and Astronomy of Uppsala University, Sweden and the Institut für Datentechnik und Kommunikationsnetze der Technischen Universität Braunschweig, Germany. The support of the national funding agencies of Germany (DLR), Italy (ASI), France (CNES), Spain (MEC), Sweden (SNSB) and the ESA Technical Directorate is gratefully acknowledged. We thank the ESA teams at ESAC, ESOC and ESTEC for their work in support of the *Rosetta* mission.

REFERENCES

Agarwal J. et al., 2016, MNRAS, 462, S78
Barucci M. A. et al., 2016, A&A, 595, A102
Cremonese G. et al., 2016, A&A, 588, A59
Davidsson B. J. R. et al., 2015, A&A, 583, A16
DeMeo F. E., Carry B., 2013, Icarus, 226, 723
Duda R. O., Hart P. E., 1973, Pattern Classification and Scene Analysis. Wiley, New York
Fink U., Rinaldi G., 2015, Icarus, 257, 9
Fornasier S. et al., 2015, A&A, 583, A30
Fornasier S. et al., 2016, Science, 354, 1566
Fulle M. et al., 2015, A&A, 583, A14
Fulle M. et al., 2016, ApJ, 821, 19
Gicquel A. et al., 2016, MNRAS, 462, S57
Jewitt D., Meech K. J., 1986, ApJ, 310, 937
Keller H. U. et al., 2007, Space Sci. Rev., 128, 433
Kelley M. S., Lindler D. J., Bodewits D., A'Hearn M. F., Lisse C. M., Kolokolova L., Kissel J., Hermalyn B., 2013, Icarus, 222, 634
Kramer T., Noack M., 2015, ApJ, 813, L33
La Forgia F. et al., 2015, A&A, 583, A41
Lai I.-L. et al., 2016, EGU General Assembly Conference Abstracts, 18, 3655
Oklay N. et al., 2016, A&A, 586, A80
Poch O., Pommerol A., Jost B., Carrasco N., Szopa C., Thomas N., 2016, Icarus, 266, 288
Pommerol A. et al., 2015, A&A, 583, A25
Rotundi A. et al., 2015, Science, 347, aaa3905
Thomas N. et al., 2015, A&A, 583, A17
Tubiana C. et al., 2015, A&A, 583, A46

[1]*INAF-Astronomical Observatory of Padova, Vicolo dell'Osservatorio 5, I-35122 Padova, Italy*
[2]*Dipartimento di Fisica e Astronomia 'G. Galilei', University of Padova, Vicolo dell'Osservatorio 3, I-35122 Padova, Italy*
[3]*CNR-IFN UOS Padova LUXOR, via Trasea 7, I-35131 Padova, Italy*
[4]*University of Olbdenburg, Ammerländer Heerstraße 114, D-26111 Oldenburg, Germany*
[5]*Max-Planck-Institut für Sonnensystemforschung, Justus-von-Liebig-Weg 3, D-37077 Göttingen, Germany*
[6]*Laboratoire d'Astrophysique de Marseille, UMR 7326 CNRS & Aix Marseille Université, 38 rue Frédéric Joliot-Curie, F-13388 Marseille cedex 13, France*
[7]*Centro de Astrobiologia, CSIC-INTA, E-28850 Torrejon de Ardoz, Madrid, Spain*
[8]*International Space Science Institute, Hallerstraße 6, CH-3012 Bern, Switzerland*
[9]*Scientific Support Office, European Space Research and Technology Centre/ESA, Keplerlaan 1, Postbus 299, NL-2201 AZ Noordwijk ZH, the Netherlands*
[10]*Department of Physics and Astronomy, Uppsala University, Box 516, SE-75120 Uppsala, Sweden*
[11]*PAS Space Research Center, Bartycka 18A, PL-00716 Warszawa, Poland*
[12]*Institut für Geophysik und extraterrestrische Physik, TU Braunschweig, D-38106 Braunschweig, Germany*
[13]*Department of Astronomy, University of Maryland, College Park, MD 20742-2421, USA*
[14]*LESIA, Observatoire de Paris, PSL Research University, CNRS, Sorbonne Universités, Univ. Paris Diderot, Sorbonne Paris Cité, UPMC Univ. Paris 06, 5 Place J. Janssen, F-92195 Meudon Principal Cedex, France*
[15]*LATMOS, CNRS/UVSQ/IPSL, 11 Boulevard d'Alembert, F-78280 Guyancourt, France*
[16]*Department of Industrial Engineering, University of Padova, Via Venezia 1, I-35131 Padova, Italy*
[17]*University of Trento, via Sommarive 9, I-38123 Trento, Italy.*
[18]*Center of Studies and Activities for Space (CISAS) 'G. Colombo', University of Padova, Via Venezia 15, I-35131 Padova, Italy*
[19]*INAF Osservatorio Astronomico di Trieste, Via Tiepolo 11, I-34014 Trieste, Italy*
[20]*Aix Marseille Université CNRS LAM (Laboratoire d'Astrophysique de Marseille), UMR 7326, F-13388 Marseille, France*
[21]*Instituto de Astrofísica de Andalucía-CSIC, E-18008 Granada, Spain*
[22]*Deutsches Zentrum für Luft- und Raumfahrt (DLR), Institut für Planetenforschung, Rutherfordstraße 2, D-12489 Berlin, Germany*
[23]*Graduate Institute of Astronomy, National Central University, 300 Chung-Da Rd, Chung-Li 32054, Taiwan*
[24]*Operations Department, European Space Astronomy Centre/ESA, P.O. Box 78, E-28691 Villanueva de la Canada, Madrid, Spain*
[25]*Geosciences Department, University of Padova, Via G. Gradenigo 6, I-35131 Padova, Italy*
[26]*Department of Information Engineering, University of Padova, via Gradenigo 6/B, I-35131 Padova, Italy*
[27]*NASA Ames Research Center, Moffett Field, CA 94035, USA*
[28]*Physikalisches Institut der Universität Bern, Sidlerstr. 5, CH-3012 Bern, Switzerland*

This paper has been typeset from a TEX/LATEX file prepared by the author.